International Forum on Aeroelasticity and Structural Dynamics
IFASD 2022
13-17 June 2022, Madrid, Spain

DATA DRIVEN AND MODEL-BASED VERTICAL SLOSHING REDUCED ORDER MODELS FOR AEROELASTIC ANALYSIS

Francesco Saltari[1], Joe J. De Courcy[2], Marco Pizzoli[1], Lucian Constantin[2], Franco Mastroddi[1], Giuliano Coppotelli[1], Brano Titurus[2], Thomas C.S. Rendall[2], Jonathan E. Cooper[2], Francesco Gambioli[3]

[1] Dept. of Mechanical and Aerospace Engineering,
Sapienza University of Rome
Via Eudossiana 18, 00184 Rome, Italy
francesco.saltari@uniroma1.it

[2]University of Bristol
Department of Aerospace Engineering
Bristol, BS8 1TR, United Kingdom
j.decourcy@bristol.ac.uk

[3]Airbus Operations Ltd
Loads & Aeroelastics Department
Filton, Bristol BS34 7PA, United Kingdom
francesco.gambioli@airbus.com

Keywords: vertical sloshing, reduced order models, aeroelasticity, neural networks, equivalent mechanical models, surrogate modelling

Abstract: A thorough understanding of the effects of sloshing on aircraft dynamic loads can be exploited for the future design of aircraft to be able to reduce their structural mass. Indeed, the high vertical accelerations caused by the vibrations of the structure can lead to the fragmentation of the fuel free surface. Fluid impacts on the tank roof are potentially a new source of damping for the structure that have hardly been considered before when computing the dynamic loads of the wings. This work aims at applying recently developed reduced-order models for vertical sloshing to a representative aeroelastic testbed, to investigate their effects on the wing's response under pre-critical and post-critical conditions. The vertical sloshing dynamics is considered comparing three different reduced order models based, respectively, on neural networks, equivalent mechanical model, and surrogate model then integrated into the aeroelastic system.

1 INTRODUCTION

The wings of civil aircraft are flexible structures that can deform significantly when withstanding atmospheric turbulence or gust loads. In these cases, the fuel contained in the wing tanks gives rise to vertical sloshing dynamics. When the structure is subjected to high vertical accelerations, the fuel starts to move inside the tanks, eventually impacting their internal walls. Therefore, liquid dynamics are coupled with aircraft structural dynamics and aeroelasticity and generally provide an increase in the overall structural damping.

In this regard, the development of reduced order models can enhance the design phase of modern aircraft.

This article aims to present the latest results concerning the application of vertical sloshing reduced-order models (ROMs) obtained within the European H2020 project SLOshing Wing Dynamics (SLOWD) (Ref. [1]) integrated within representative aerolastic models. The complexity in modelling this phenomenon lies in the peculiar dissipative behaviour in which Rayleigh-Taylor (Ref. [2]) instabilities occur when the vertical acceleration (perpendicular to the free surface of the liquid) imposed on the tank exceeds a certain threshold causing a chaotic regime with continuous mixing of liquid and air. In addition, turbulence, impacts with the tank walls and continuous free surface generation cause additional dissipation of energy (Refs. [3–5]). The overall balance of elastic potential energy and fluid energy leads to a noticeable increase in the effective damping of the structural motion.

It is worth emphasising that, vertical sloshing is not the only dynamic that can affect the aeroelastic system. In fact, depending on the type and intensity of the perturbations to which the aircraft is subjected, sloshing can exhibit different behaviours. Rotations and lateral motions of tanks, in which the liquid generally presents standing waves within the cavity, provides dynamic coupling with the structure and a possible change in the aeroelastic dynamic stability margin. The effects of this type of sloshing on the aeroelastic flutter stability of aircraft have been discussed in Refs. [6–8] where liquid dynamics was modelled using equivalent mechanical models (EMMs), frozen fluids and linear frequency domain approaches. Furthermore, the effects of sloshing on aeroelastic typical section behaviour has been investigated in Refs. [9, 10] by direct time-marching analysis employing Smoothed Particle Hydrodynamics (SPH).

In this work, an aeroelastic model containing two tanks of the same dimensions is considered to simulate and study the effects induced on its response by vertical sloshing. Specifically, two aeroelastic methodologies exploiting three different types of reduced order models for sloshing are compared.

The first approach involves the use of equivalent mechanical models to replace the dynamics of vertical sloshing. We refer in particular to a bouncing ball model, designed to emulate the impact mechanism of the phenomenon under investigation. This has been previously used to replicate transient experimental response through two independently formulated models [5, 11], showing good correlation with the global dissipative behaviour. Aeroelastic studies in which sloshing was modelled with this kind of ROM can be found in Ref. [12] where the damping performance of the aeroelastic/sloshing system was characterised as gust speed and intensity varied. The bouncing ball address the need to describe the complex liquid dynamics through a simple physical model quickly and effectively.

Following this, a surrogate model for vertical fluid sloshing based on the direct interpolation of experimental data is developed. Radial basis function interpolation is used to provide a smooth representation of hydrodynamic force measurements taken from vertical harmonic excitation of a fluid-filled tank [13]. This methods ensures a smooth and continuous function for use in numerical models, that exactly recovers experimental data. Furthermore, this method can be used directly with harmonically excited sloshing data and requires no calibration or pre-processing stage.

The third methodology, which follows what has already been presented in [14], involves the use of nonlinear systems identification techniques based on neural networks. They are a powerful tool for approximating nonlinear dynamic systems, even when the structure of the system to be identified is unknown and only input–output data are available, so allowing a sort of generalised black-box modelling. This work makes use of a Nonlinear Finite Impulse Response (NFIR)

	$y_{T_i}[m]$	$h^{(i)}[m]$	$V^{(i)}[m^3]$	α
tank 1	4.90 $(0.8L)$	0.08	0.05	0.50
tank 2	5.70 $(0.93L)$	0.08	0.05	0.50

Table 1: Parameters of the tanks: position of the geometric centre with respect to the y-axis y_{T_i}, tank height $h^{(i)}$, volume $V^{(i)}$ and filling level α.

network trained with an appropriate data series obtained by a suitable scaled experiment (see Ref. [15]) spanning different values of frequencies and displacement amplitude. In addition, a scaling law is implemented to adapt the model to the geometry of the wing tanks. The three different approaches will be compared by assessing the effects they introduced in the response of the considered aeroelastic system.

2 AEROELASTIC/SLOSHING FORMULATION

A sloshing/aeroelastic wing is modelled in this work using a hybrid model that combines a linear differential problem (aeroelasticity) with sloshing models that can be data-driven or equivalent mechanical models. More in details, the numerical testbed is represented by the Goland wing model (Ref. [16, 17]) in which two tanks partially filled with liquid with characteristics listed in Tab. 1 are integrated. Figure 1 shows the 1D structural model, along with the lifting surface discretized by means of strip theory, and the position of the two tanks lying on the elastic axis of the wing. Figure 2 shows the wing first six modes of vibration in the case of *dry* structure.

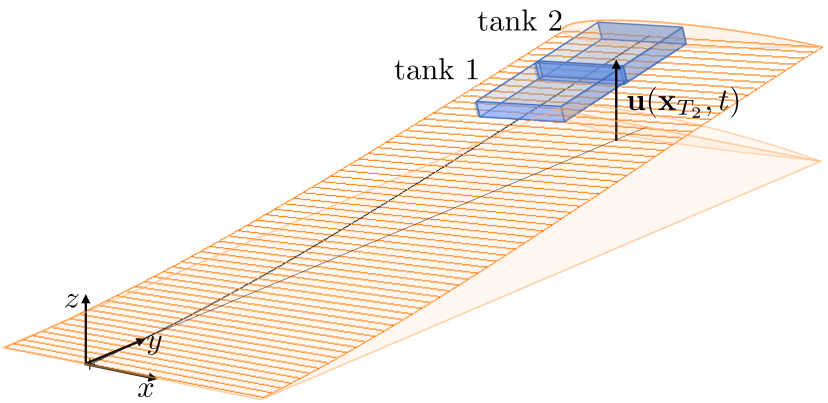

Figure 1: Goland wing aeroelastic/sloshing modelling.

A box-shaped, rigid structure is approximated for both the tanks embedded within the wing-box. Their dynamic behaviour is condensed in a point placed in the tank geometric centre.

The wing structural displacements $\mathbf{u}(\mathbf{x}, t)$ can be expressed by the spectral decomposition

$$\mathbf{u}(\mathbf{x}, t) \simeq \sum_{n=1}^{N} \boldsymbol{\psi}_n(\mathbf{x}) q_n(t) \tag{1}$$

where $\boldsymbol{\psi}_n(\mathbf{x})$ are the modes of vibrations of the structure and $q_n(t)$ are the generalised coordinates describing the body deformation in time. Note that a space-discretization for the structure is assumed by including a finite number N of modes in the analysis, *i.e.,* a frequency-band-limited unsteady process. Considering this representation for aircraft wing dynamics, one has the following Lagrange equations of motion in terms of N modal coordinates $q_n(t)$

$$\mathsf{M}\ddot{\mathsf{q}} + \mathsf{K}\mathsf{q} = \mathsf{e} + \mathsf{g} + \mathsf{f}^{(ext)} \tag{2}$$

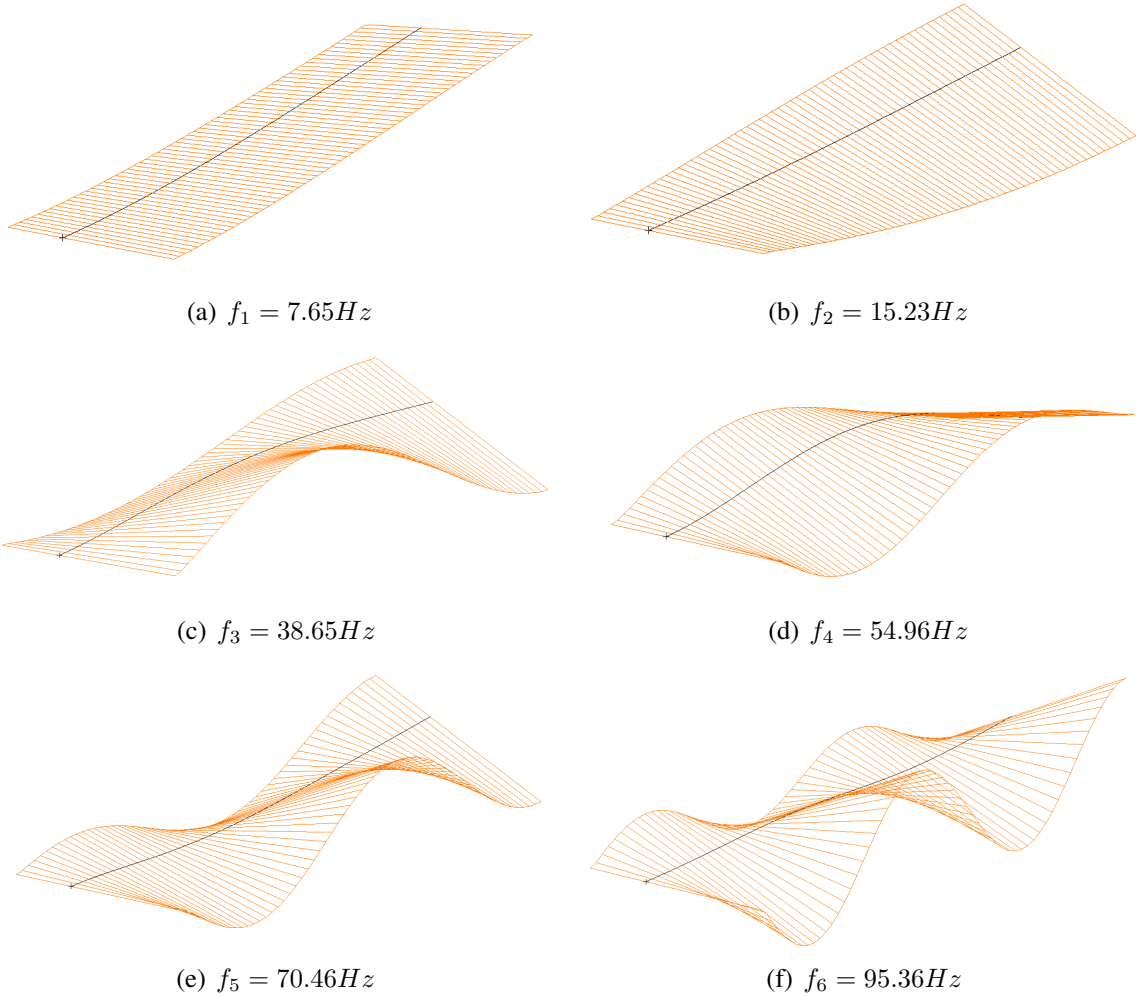

(a) $f_1 = 7.65Hz$ (b) $f_2 = 15.23Hz$

(c) $f_3 = 38.65Hz$ (d) $f_4 = 54.96Hz$

(e) $f_5 = 70.46Hz$ (f) $f_6 = 95.36Hz$

Figure 2: Mode shapes of the wing model with their natural frequencies.

where $\mathsf{q} = [q_1, q_2, \ldots, q_N]^{\mathrm{T}}$ is the modal coordinates vector, M and K are, respectively, the modal mass and stiffness (diagonal) matrices (provided by a FEM solver or the analytical solution given by the beam theory), whereas $\mathsf{e} = [e_1, e_2, \ldots, e_N]^{\mathrm{T}}$ and $\mathsf{g} = [g_1, g_2, \ldots, g_N]^{\mathrm{T}}$ are, respectively, the generalized *aerodynamic* and *sloshing* forces induced by the elastic motion. The $\mathsf{f}^{(ext)}$ is the vector of the current external forcing terms which includes gust loads. The generalized aerodynamic forces (due to the aircraft motion only) are generally computed as a function of the reduced frequency $k = \omega b/U_\infty$ (with b semi-chord and U_∞ free stream velocity) and Mach M_∞ domain (see Ref. [18]) as:

$$\tilde{\mathsf{e}} = q_D \, \mathsf{Q}(k, M_\infty) \, \tilde{\mathsf{q}} \tag{3}$$

where $\mathsf{Q}(k, M_\infty)$ is the generalised aerodynamic forces matrix, q_D is the dynamic pressure and the symbol $\tilde{}$ is used to represent the Laplace/Fourier transforms. For a fixed value of M_∞, the unsteady aerodynamics can generally be recast in time domain as:

$$\mathsf{e} = q_D \, \mathsf{A}_0 \, \mathsf{q} + q_D \, \frac{b}{U_\infty} \, \mathsf{A}_1 \, \dot{\mathsf{q}} + q_D (\frac{b}{U_\infty})^2 \, \mathsf{A}_2 \, \ddot{\mathsf{q}} + q_D \, \mathsf{C} \, \mathsf{r} \tag{4}$$

$$\mathsf{E}\dot{\mathsf{r}} = \frac{U_\infty}{b} \, \mathsf{P} \, \mathsf{r} + \mathsf{B} \, \dot{\mathsf{q}} + \mathsf{D}\ddot{\mathsf{q}} \tag{5}$$

where b is the reference half-chord and r is the vector of the aerodynamic finite states. Depending on the aerodynamic model and rational function approximation, matrices E and D are set

to the identity and null matrix, respectively, within Sec. 3.2. Or alternatively follow from the Peters' finite-state model [19] as per Sec. 3.1.

At the same time, the generalised sloshing forces vector g can be expressed as a sum of contributions $\mathsf{g}^{(i)}$ of individual tanks:

$$\mathsf{g} = \sum_{i=1}^{N_T} \mathsf{g}^{(i)} \tag{6}$$

with N_T the number of tanks. The *n-th* component of $\mathsf{g}^{(i)}$ is the projection of the fluid pressure distribution p_S evaluated on the wet tank surface $\mathcal{S}_{tank}^{(i)}$ on each *n-th* modal shape $\boldsymbol{\psi}_n$ as in the following ($\mathbf{n}$ unit normal vector to $\mathcal{S}_{tank}^{(i)}$)

$$g_n^{(i)} = -\oiint_{\mathcal{S}_{tank}^{(i)}} p_S \; \mathbf{n} \cdot \boldsymbol{\psi}_n \, d\mathcal{S} \tag{7}$$

By assuming a rigid tank identified by its geometrical centre in which the moment about the tank geometric centre are negligible and the sloshing force lies mainly in the vertical direction, Eq. 7 can be recast as:

$$g_n^{(i)} = \mathbf{i}_3 \cdot \boldsymbol{\psi}_n(\mathbf{x}_{T_i}) F_S^{(i)} \tag{8}$$

where $\mathbf{i}_3$ is the vertical unit vector and $F_S^{(i)}$ is the component of the vertical sloshing force. In this study, the sloshing force can be decomposed into two contributions: the inertial force according to the frozen fuel modelling (Ref. [7]) and the perturbation resulting from the relative motion of the fluid particles within the tank (Ref. [20]) providing:

$$F_S^{(i)} \;\; = \;\; -\sum_{k=1}^{N} m_l^{(i)} \mathbf{i}_3 \cdot \boldsymbol{\psi}_k(\mathbf{x}_{T_i}) \ddot{q}_k + \Delta f_{S_z}^{(i)} \tag{9}$$

where $\Delta f_{S_z}^{(i)}$, hereafter denoted as *dynamic sloshing force* is a non-conservative force that is a nonlinear function of the history of the tank vertical displacement $u_z(\mathbf{x}_{T_i}, t)$. Based on Eq. 9 Eq. 8 can be recast as:

$$g_n^{(i)} = m_{L_{nk}}^{(i)} \ddot{q}_k + \mathbf{i}_3 \cdot \boldsymbol{\psi}_n(\mathbf{x}_{T_i}) \, \Delta f_{S_z}^{(i)} \tag{10}$$

where the components $m_{L_{nk}}$ provides a further non-diagonal contribution to the mass matrix given by the inertia of the fluid. Recast in state space, Eqns. 4 and 10 take the form

$$\begin{bmatrix} \mathsf{I} & 0 & 0 \\ 0 & \mathsf{M} + \mathsf{M}_L - q_D \left(\frac{b}{U_\infty}\right)^2 \mathsf{A}_2 & 0 \\ 0 & \mathsf{D} & -\mathsf{E} \end{bmatrix} \begin{Bmatrix} \dot{\mathsf{q}} \\ \ddot{\mathsf{q}} \\ \dot{\mathsf{r}} \end{Bmatrix} + \begin{bmatrix} 0 & -\mathsf{I} & 0 \\ \mathsf{K} - q_D \frac{b}{U_\infty} \mathsf{A}_1 & -q_D \mathsf{A}_0 & q_D \mathsf{C} \\ 0 & \mathsf{B} & \frac{U_\infty}{b} \mathsf{P} \end{bmatrix} \begin{Bmatrix} \mathsf{q} \\ \dot{\mathsf{q}} \\ \mathsf{r} \end{Bmatrix} = \begin{Bmatrix} 0 \\ \sum_i^{N_t} \mathsf{b}^{(i)} \Delta f_{S_z}^{(i)} \\ 0 \end{Bmatrix} \tag{11}$$

where $\mathsf{b}^{(i)} = [\mathbf{i}_3 \cdot \boldsymbol{\psi}_1(\mathbf{x}_{T_i})], \ldots, \mathbf{i}_3 \cdot \boldsymbol{\psi}_N(\mathbf{x}_{T_i})]^\mathsf{T}$ is a vector that collects the vertical displacement of the vibration modes evaluated at the *i-th* tank position.

Three methods will be used to investigate the response of a sloshing aeroelastic wing, namely: *i)* a bouncing ball model, where the interaction between the fluid and structure is mirrored in the reaction forces between a ball and the tank walls (described in Sec. 2.1), *ii)* a surrogate model based on interpolation of experimental data (Sec. 2.2), and *iii)* a neural network-based ROM in which the sloshing forces are derived from an identified black box (covered in Sec. 2.3).

2.1 Bouncing ball model

Previous work by the authors have noted that a simple rigid mass moving under vertical excitation can provide surprisingly representative sloshing behaviour and dissipative characteristics. Such equivalent mechanical models have been investigated in the purely vertical single-degree-of-freedom case under large amplitude excitation, in both the transient [5, 11] and prescribed [13] motion cases. Following from this analysis, an equivalent mechanical model based on a ball bouncing inside a tank was applied to loads alleviation studies in the aeroelastic setting [12]. Where visco-elastic impacts of the ball with tank boundaries dissipate energy and drive the fluid motion in the coupled system. The bouncing ball model subsequently presented here is an extension of that particular work.

This model makes the assumption that a fluid may be treated a singular rigid mass that travels in a ballistic path during a free-flight period, before elastic impact with the containing vessel. This limits the ability to capture free surface effects, in particular any surface waves (i.e. parametric sloshing below 1g acceleration excitation) or surface fragmentation. In doing so, fluid is discretised as a single point mass (m_l) which moves vertically with absolute position u_b, which is introduced as an additional state in the aeroelastic system. The vertical extent of the particles motion is limited by visco-elastic barrier functions which act at the tank boundaries (floor and roof) at $[-U_f, U_f] + u_t$, where u_t is the vertical displacement of the wing at the tank centre. The geometric constant U_f is the 'free-flight' range of the fluid set by tank height and fluid filling ratio, specifically $U_f = 0.5(1 - \text{fill})H_t$. Barrier functions are composed of two elements, an elastic and smooth barrier force, shown in Fig. 3 and defined as

$$F_{sb}(r) = \frac{K_u}{\pi}\left[(r+U_f)\left(\frac{\pi}{2} + \tan^{-1}\frac{-(r+U_f)}{\epsilon_s}\right) + (r-U_f)\left(\frac{\pi}{2} + \tan^{-1}\frac{(r-U_f)}{\epsilon_s}\right)\right] \tag{12}$$

where $r = u_b - u_t$ is the relative position of the ball from the tank position on the wing. ϵ_s controls the smoothness of the region between free-flight and barrier conditions as shown in Fig. 3(a). Wall stiffness K_u and ϵ_s are mainly set to ensure the fluid is sufficiently retained within the free-flight distance U_f during impacts, whilst ensuring a 'soft' impact that to minimise the excitation of high-frequency modes in the coupled system. As shown in Fig. 3(b), the damping function includes a smoothed activation of the non-conservative force in the vicinity of the wall barrier

$$F_{cb}(r, \dot{r}) = f_1(r) C_u \dot{r}, \quad f_1(r) = \left[\phi(r) H(U_f - |r|) + H(|r| - U_f)\right] H(|r| - (U_f - \epsilon_D)) \tag{13}$$

where H is the heaviside function, C_u the damping constant ($2\zeta\sqrt{m_l K_u}$) and ϕ an interior smoothing function

$$\phi(R) = (1-R)_+^4(4R+1), \quad R = (U_f - |r|)/\epsilon_D \tag{14}$$

Included with these nonlinear barrier functions, weight of the fluid is included to drive the ball in a ballistic flight in the interior free-flight region and ensure repeated impacts with the tank as the wing settles. Therefore, equations of motion for each EMM take the simple form

$$m_l \ddot{u}_b = m_l g - F_{sb} - F_{cb} \tag{15}$$

Section 3.1 describes how this EMM is introduced into the aeroelastic framework and how the sloshing forces are distributed onto the structure. It is noted that this model can provide sensible dissipation characteristics and fluid-structure interactions, but may struggle to exactly match experimental characteristics without calibration [5]. Despite this, the ballistic nature of the model implies no restriction on the frequency and amplitude of excitation, given the acceleration is above 1g which is required for the ball to be released from the wing.

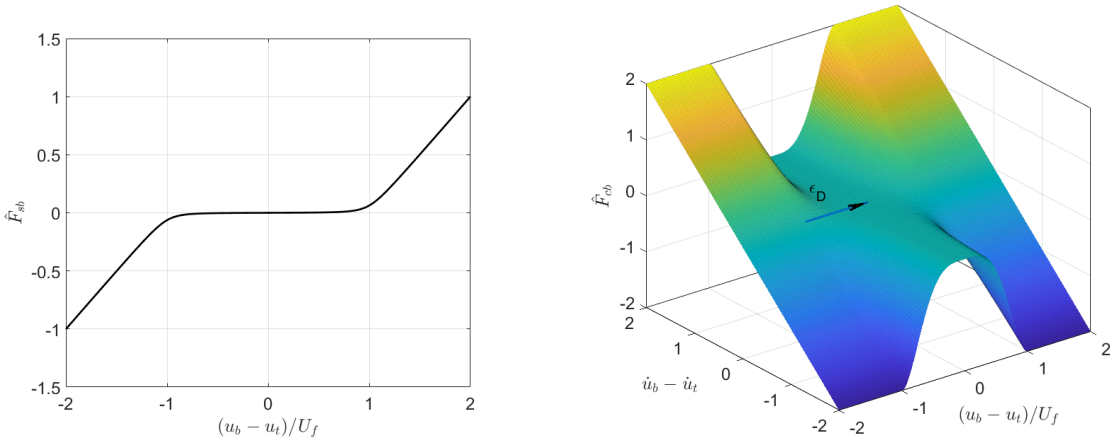

(a) Barrier stiffness (b) Barrier damping

Figure 3: Visco-elastic functions used in bouncing ball sloshing model

2.2 Surrogate sloshing model

Within the second fluid model considered, a surrogate model is developed to provide the dynamic sloshing loads on the wing structure, based upon direct interpolation of known experimental response. Response surfaces are computed which provide the quasi-steady sloshing force for a particular kinematic condition of excitation. A smooth interpolation allows for discrete experimental data to be used directly in the numerical framework, where no pre-processing or calibration phase is required. Further, the range of experimental data covers low-amplitude parametric sloshing and violent vertical sloshing, allowing the numerical model to capture these behaviours; making the assumption that the geometric tank characteristics that drive the sloshing behaviour is preserved between scales.

Previous experimental work has considered the prescribed vertical harmonic excitation of a fluid filled tank, across a series of excitation amplitudes and frequencies. For details on the experimental characteristics see Ref. [13]. For a single amplitude and frequency of excitation (for instance a single circle in the xy plane of Fig. 4) the hydrodynamic force was measured and averaged over multiple cycles, providing the quasi-steady hydrodynamic force at each kinematic condition in the cycle. From this the sloshing force is isolated by removing the inertial and hydrostatic force component, i.e. the force resulting from having a dynamic medium inside the tank. Specifically, from the total measured force F_t,

$$F_s = F_t - \ddot{u}(m_l + m_s) - g(m_l + m_s) \tag{16}$$

where m_l and m_s are the liquid and structural masses, respectively. The combination of these individual cycles over multiple amplitudes of excitation can be used to form a response surface, which provides the quasi-steady sloshing force at each kinematic state of excitation. To combine the discrete experimental data points into a smooth and continuous function that can be used within numerical analysis, a surrogate model is developed based on radial basis function (RBF) interpolation of the discrete data.

Considering non-dimensional displacement $\hat{u} = u/h$, velocity $\hat{v} = \dot{u}/(\omega h)$ and sloshing force $\hat{F}_s = F_s/(m_l h \omega^2)$, the function mapping kinematics to sloshing force takes the form $\hat{F}_s = g(\hat{\mathrm{x}})$, $\hat{\mathrm{x}} = \{\hat{u}, \hat{v}, \omega\}$. Within the previous experimental work [13], normalisation of dissipated energy via $\hat{E} = E/(m_l \omega^2 A^2)$ where A is the amplitude of harmonic excitation, was shown to provide a consistent scaling across excitation conditions. However, in the transient setting a characteristic amplitude is not known a priori, thus the characteristic length of tank height is

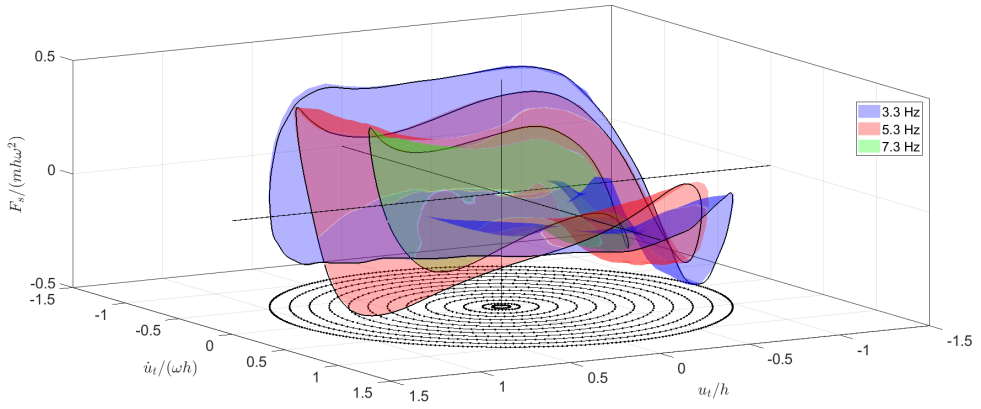

Figure 4: Interpolated experimental response surfaces. Traces on the xy-plane show experimental amplitudes for the 3.3 Hz case forming the response surface.

used within this process. The RBF interpolation, including a polynomial of any degree, provides the interpolated function values $g(\hat{\mathrm{x}})$ at an evaluation point $\hat{\mathrm{x}}_E$,

$$g(\hat{\mathrm{x}}_E) = \sum_{i=1}^{N} \gamma_i \phi(|\hat{\mathrm{x}}_E - \hat{\mathrm{x}}_i|, r) + \sum_{k=1}^{M} \beta_k q_k(\hat{\mathrm{x}}_E) \tag{17}$$

where N is the number of experimental data points, q the M monomial coefficients based on the degree of the included polynomial and dimensionality of the data and ϕ a compact basis function (a Wendland C4 is used [21]) dependent on a support length r. Model coefficients γ and β are found by requiring exact recovery of the experimental/sample points, requiring solution of the linear system

$$\begin{pmatrix} \Phi & \mathrm{Q} \\ \mathrm{Q}^{\mathrm{T}} & 0 \end{pmatrix} \begin{pmatrix} \gamma \\ \beta \end{pmatrix} = \begin{pmatrix} \mathrm{g} \\ 0 \end{pmatrix} \tag{18}$$

where details of this process can be found in most RBF interpolation references, for instance Ref. [21]. This interpolation ensures the experimental data points are exactly recovered, and returns to a least-squares polynomial fit in the absence of RBF influence. Additionally, to improve matrix conditioning and simplify dependence on support radius r, the experimental domain ($\hat{\mathrm{x}}_i, i = 1, ..., N$) is scaled to the hypercube. Ultimately, the surrogate model forms the operator G, which is introduced into the aeroelastic model in the form

$$\Delta f_{S_z}^{(i)} = m_l^{(i)} h^{(i)} \omega_c^2 G \left(\frac{\mathbf{u}(\mathbf{x}_{T_i}, t)}{h^{(i)}}, \frac{\dot{\mathbf{u}}(\mathbf{x}_{T_i}, t)}{\omega_c h^{(i)}}, \omega_c \right) \tag{19}$$

where ω_c is a characteristic frequency chosen dependent on the dominate excitation component, i.e. first bending of the aeroelastic system in free-stream conditions. Noting this sloshing model therefore does not dynamically respond to the frequency of excitation from the aeroelastic input. A series of interpolated response surfaces are shown in Fig. 4, where the experimental data points for one frequency of excitation are shown on the xy axis.

2.3 Neural-network-based reduced order model

The third reduced-order model considered is based on a neural network trained directly with experimental data, using the same approach as presented in Ref. [20]. Specifically, the model is identified by exploiting the experimental data obtained from the set-up introduced in Ref. [15] to investigate the dissipative behaviour of the fluid sloshing inside a tank set in vertical motion.

This experimental configuration consists of a box tank (with a height of $h = 27.2$ mm and base of sides $l_1 = 117.2$ mm and $l_2 = 78.0$ mm) placed over a controlled electrodynamic shaker able to impose vertical sinusoidal displacement. The dynamic load at the interface between shaker and tank is measured by two load cells, placed in the middle of the long side of the tank base. The system is also equipped with two accelerometers placed at the opposite corners of the tank upper closing side and with a control accelerometer used by the shaker controller. Figure 5(a) provides the non-dimensional energy dissipated by the sloshing fluid $\hat{E} = E/(m_l A^2 \Omega^2)$ in a vertical harmonic motion $u_z = A\cos(\Omega t)$ (with A displacement amplitude of the imposed motion and Ω the excitation frequency) as a function of the non-dimensional frequency $\bar{\omega} = \Omega/\sqrt{g/h}$ and velocity $\bar{v} = v/\sqrt{gh}$ (with $v = \Omega A$). Note that different non-dimensional

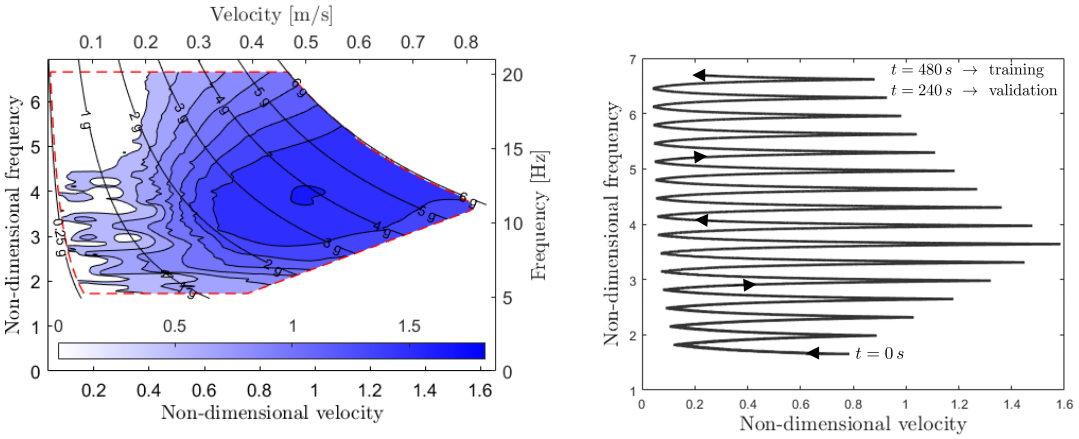

(a) Maps of the Identified dissipated energy

(b) Velocity path in non dimensional frequency-amplitude domain

Figure 5: Experimental dissipated energy map and path considered for training data generation

quantities are defined for the neural network in this section with respect to Sec. 2.2. Therefore the new non-dimensional quantities are here denoted by means of $\bar{}$. Subsequently, the experimental set-up was used to generate a data set for training a neural network by means of a $480\,s$ long test with a variable frequency and amplitude harmonic imposed acceleration $\ddot{u}_z = f(t)\cos(\int \Omega(t)\mathrm{d}t)$ such as to suitably cover the frequency-velocity domain of interest (see Fig. 5(b)). A different data set $240\,s$ long covering the same points in the frequency-velocity domain is used for validation in order to avoid overfitting of training data. Figure 6 shows the vertical velocity of the tank obtained by integrating the acceleration signal, that is the input feeding the network, whereas, the dynamic sloshing forces, estimated by the load cells subtracting the frozen fluid and tank masses inertia is shown in Fig. 7. Among the wide vari-

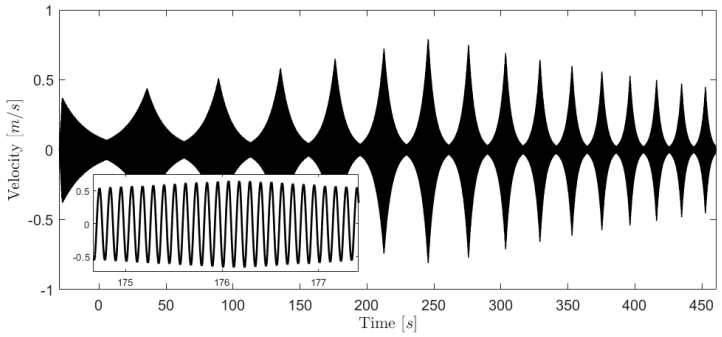

Figure 6: Time history of the velocity profile used to train the network, see Ref. [20]

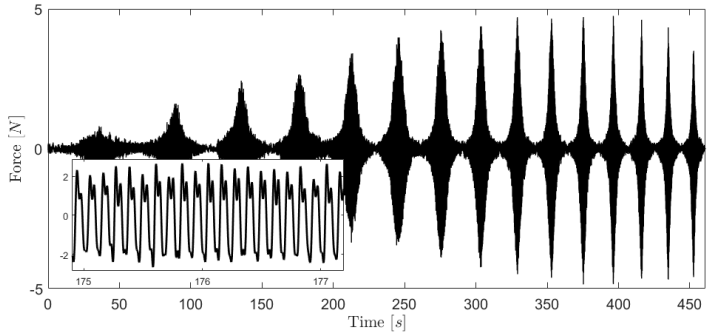

Figure 7: Time history of the dynamic sloshing forces for the training data set

ety of dynamical models, a neural-network-based nonlinear finite impulse response (NN-NFIR) model has been selected (see Fig. 8). NFIR models, simply made up by static approximator

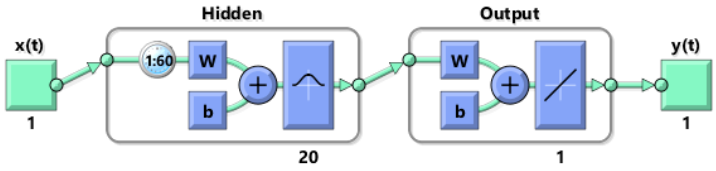

Figure 8: Time-Delay Neural Network flowchart

(neural network) and a bank of filters with delay lines, generally ensures the stability of the reduced order model (Ref. [22]). The used NN-NFIR model consists of 1 hidden layer with 20 neurons and 1 output layer whilst 60 tapped delay lines are considered for the input. Normalised radial basis functions are employed as activation functions in all nodes of the hidden layer, whereas the output layer is made up with a simple linear function. The model identified in this study was trained in Matlab® (Ref. [23]) using an error rate increase criterion over 6 consecutive epochs as the stopping criterion. The stopping of the training process occurred after 76 epochs, when the mean-squared error performance had already stabilised at a constant and relatively low value. The trained network was then converted into a Simulink® block to be used for simulations and thus obtaining predictions for the output.

The tanks implemented in Goland's wing model have different dimensions to those of the box used to generate the training data for the neural network (see Tab. 1). In order to exploit the reduced order model presented in this section, the scaling procedure introduced in Ref. [14] is used. Since the operational parameters $\bar{\omega}$ and $\bar{v}$ only cover a subspace of the space spanned by the non-dimensional parameters influencing the sloshing-induced energy dissipation, it is necessary to formulate the following hypotheses before scaling the NN-based ROM:

- The non-dimensional sloshing force, defined as $\phi = f_{S_z}/(m_l A\Omega^2)$, is assumed to be mainly dependent on the non-dimensional velocity (Froude) and non-dimensional frequency (or non-dimensional time).
- The principal dimension is assumed to be the tank height h (Ref. [24]).
- For each filling level α a different identification is required.

The re-scaled ROM must therefore work in similarity of $\bar{v}$ and $\bar{\omega}$ as well as non-dimensional sloshing force ϕ in order to replace the sloshing model with a neural network capable of reproducing the real dissipative behavior. Figure 9 shows the Simulink® implementation of the neural network unit and the scaling gain. More in details, from the non-dimensional frequency

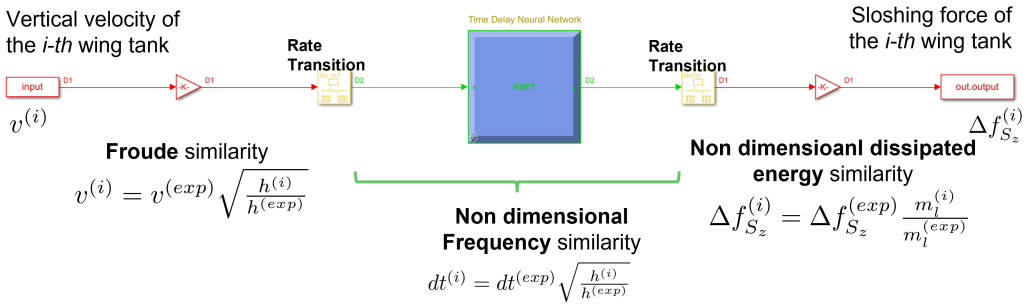

Figure 9: Scaling procedure implemented in Simulink®.

similarity between the experiment $\bar{\omega}^{(exp)}$ and the *i-th* tank $\bar{\omega}^{(i)}$, we obtain the scaling for the time sampling $dt^{(i)}$. A proper time rate transition block is used within the simulation (see Fig. 9) to make the neural network working with a time rate compliant with the one used for its identification. Furthermore, the similarity of the non-dimensional velocity of the vertical motion provides a gain to the vertical tank velocities $v^{(i)}$ before the call to the neural network (see Fig. 9). From the similarity of the non-dimensional sloshing force ϕ, we obtain the gain for the dynamic sloshing $\Delta f_{S_z}^{(i)}$ forces to be applied after the call to the neural network within the simulation framework (see Fig. 9). In this scaling procedure, velocity and displacements of the tank are adjusted according to tank size, but the maximum accelerations achievable when the tank works in similarity with the tank used for the network identification are retained.

3 NUMERICAL FRAMEWORKS

This section introduces the numerical frameworks used to perform numerical simulation of the sloshing/aeroelastic response of the Goland wing. More specifically, two numerical framework are described, that is the one from the *University of Bristol* in which the sloshing dynamics is described by means of the bouncing ball model or the surrogate sloshing model and the one from *Sapienza University of Rome* in which sloshing is described by means of neural networks.

3.1 University of Bristol

Within this particular approach, the aeroelastic model of Fazelzadeh *et al.* [17] is used for coupling with the bouncing ball and surrogate fluid models. Structural dynamics is modelled with the classical beam theory, including linear torsion and bending response only. Unsteady aerodynamics is accounted for using Peters' finite state model [19], which is an extension of strip theory to capture unsteady wake effects in a set of finite induced-flow states. The Galerkin method is used to discretise the structural dynamics within a set of assumed shape functions. The global equations of motion for the aeroelastic case, including sloshing forces from the surrogate model take the form of Eqn. 11. Where M_L is the liquid inertia matrix, A_{0-2} strip theory aerodynamics terms and matrices E, D, B and P arising from the Peters' finite state model, applying additional forcing from the inflow states via C. Hydrodynamic loading from the surrogate model at each tank is computed via equation 19 and applied as point loads at the tank centre.

Additionally, when the bouncing ball model is used the fluid displacement is introduced into the state vector as additional mechanical states $\mathsf{u}_b = \{u_b^1, ..., u_b^{N_t}\}^T$ as within Eqn. 21. In this form, liquid inertia is applied within the EMM equations of motion rather than the aeroelastic

model, via the diagonal mass matrix

$$\mathsf{M}_l = \begin{Bmatrix} m_l^1 & 0 & 0 \\ 0 & \ddots & 0 \\ 0 & 0 & m_l^{N_t} \end{Bmatrix} \tag{20}$$

$$\begin{bmatrix} \mathsf{I} & 0 & 0 & 0 & 0 \\ 0 & \mathsf{M} - q_D \left(\frac{b}{U_\infty}\right)^2 \mathsf{A}_2 & 0 & 0 & 0 \\ 0 & \mathsf{D} & -\mathsf{E} & 0 & 0 \\ 0 & 0 & 0 & \mathsf{I} & 0 \\ 0 & 0 & 0 & 0 & \mathsf{M}_l \end{bmatrix} \begin{Bmatrix} \dot{\mathsf{q}} \\ \ddot{\mathsf{q}} \\ \dot{\mathsf{r}} \\ \dot{\mathsf{u}}_b \\ \ddot{\mathsf{u}}_b \end{Bmatrix} + \\ \begin{bmatrix} 0 & -\mathsf{I} & 0 & 0 & 0 \\ \mathsf{K} - q_D \frac{b}{U_\infty} \mathsf{A}_1 & -q_D \mathsf{A}_0 & q_D \mathsf{C} & 0 & 0 \\ 0 & \mathsf{B} & \frac{U_\infty}{b} \mathsf{P} & 0 & 0 \\ 0 & 0 & 0 & 0 & -\mathsf{I} \\ 0 & 0 & 0 & 0 & 0 \end{bmatrix} \begin{Bmatrix} \mathsf{q} \\ \dot{\mathsf{q}} \\ \mathsf{r} \\ \mathsf{u}_b \\ \dot{\mathsf{u}}_b \end{Bmatrix} = \begin{Bmatrix} 0 \\ \sum_i^{N_t} \left(F_i^{sb} + F_i^{cb}\right) \mathbf{i}_3 \cdot \boldsymbol{\psi}(\mathbf{x}_{T_i}) \\ 0 \\ 0 \\ \mathsf{g}_i^b(\mathsf{q}, \dot{\mathsf{q}}, \mathsf{u}_b, \dot{\mathsf{u}}_b) \end{Bmatrix} \tag{21}$$

Finally, the visco-elastic forces and equations of motion Eqns. 12-15 are computed within g_i^b, and the resulting barrier forces applied to the wing as point loads [12]. In the subsequent analysis, 3 bending and 3 torsion shapes are used, with 6 aerodynamic inflow states discretised at 10 spanwise locations. Time integration of the ODEs is performed within Matlab® using the explicit Runge-Kutta (4,5) method.

3.2 Sapienza University of Rome

The aeroelastic/sloshing modelling is implemented by Sapienza University of Rome (hereafter simply denoted by means of the acronym USRS) in a Simulink® environment as illustrated in Fig. 10. The aeroelastic blocks are purely differential whereas the sloshing block is modelled with the identified data-driven neural-network-based ROM. The simulation model implements Eq. 2, in which the sloshing forces $\mathbf{i}_3 \cdot \boldsymbol{\psi}_n(\mathbf{x}_{T_i})\, \Delta f_{S_z}^{(i)}$ are the loads predicted by the neural network, following the history of the modal velocity evaluated at the two tank positions $\mathbf{x}_{T_i}$ as equal to $\sum_m \boldsymbol{\psi}_m(\mathbf{x}_{T_i}) \dot{q}_m(t)$.
The aeroelastic system is modelled by employing the finite element method (FEM) to get the structural modes of the beam and by generating a lifting surface (see Fig. 1) based on the Theodorsen theory. However, the latter could also be generalised using the doublet lattice method (DLM) discretisation method for the unsteady aerodynamics (see Ref. [18]). The aeroelastic analysis is based on the modes of vibration of the dry structure. Based on these, the FE solver also allows for computation of the generalised aerodynamic force (GAF) matrices for Mach number and reduced frequency k pairs provided by the user. To achieve a purely differential formulation for the unsteady aerodynamics, a rational function approximation (RFA) based on Roger interpolation method (in which matrices E and D are, respectively, set to the identity and null matrix, see Ref. [25]) is applied to the GAF matrix, resulting in the definition of a new set of aerodynamic finite states. The numerical model also incorporates a block that allows the gust to be included as an external input acting on the aeroelastic system. The analyses are carried out using 20 modes of vibrations and the Roger interpolation is made considering 5 lags yielding a total of 100 aerodynamic states.

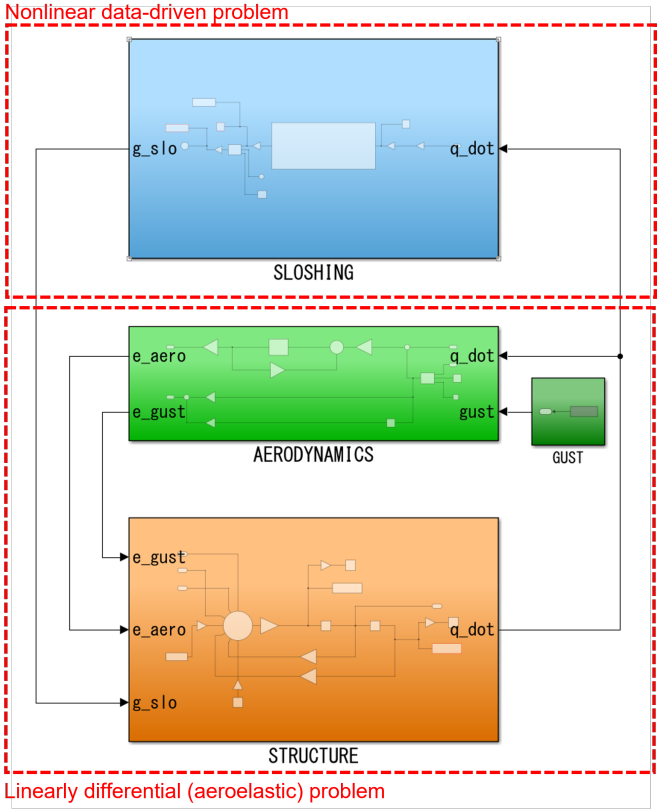

Figure 10: Aeroelastic/sloshing modelling in Simulink®.

	Flutter velocity $[m/s]$	Flutter frequency $[Hz]$
UB	$161.7(\rightarrow 165.5)$	$9.18(\rightarrow 9.35)$
USRS	163.1	9.

Table 2: Flutter velocity and frequency for the two models. Note that in parentheses it is highlighted the modification of flutter scenario due to linear sloshing, if any.

4 RESULTS

In this section, the aeroelastic response results of the beam are presented comparing the the performances of the three models. The comparisons are necessarily split in different plots (USRS model responses on the left and UB model responses on the right) since the models used by the two partners differ slightly in flutter scenario. The stability scenario (root locus) of the aeroelastic system in frozen configuration ($\Delta f_{S_z}^{(i)} = 0$) is shown in Fig. 11. The stability analysis is performed by evaluating the poles of the linearly differential aeroelastic system by varying the free stream velocity U_∞ between 100 m/s and 200 m/s and considering fixed the Mach number $M_\infty = 0$ and the air density $\rho_\infty = 1.225\,\mathrm{kg/m^3}$. Flutter occurs from the branch that originates from the first bending mode (see Fig. 2(a)) and the critical eigenvector is mainly given by the coupling from the first and second modes of vibration. Table 2 lists the flutter speed and frequency obtained from the aeroelastic frameworks developed in this activity.

Aeroelastic response analyses to vertical gust are performed for different gust amplitudes and different velocities. Specifically, in this analyses we consider the following standard gust profile:

$$w_g(t) = \frac{1}{2} w_{g_a} \left(1 - \cos\left(\frac{2\pi U_\infty t}{L_g}\right)\right) \tag{22}$$

where w_{g_a} is the gust amplitude. The reference value for the gust length measured in chord

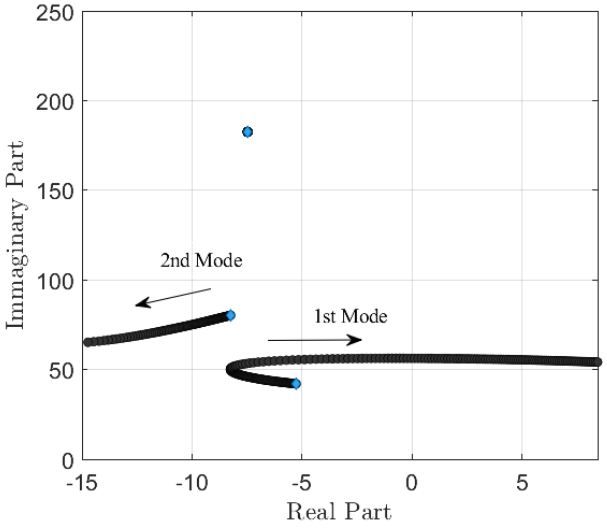

Figure 11: USRS Root locus of the aeroelastic system in frozen configuration ($\Delta f_{S_z}^{(i)} = 0$).

length b is $L_g = 25\,b$. Spatially, the gust is assumed to be constant throughout the wing domain. Two configurations are compared, namely the *frozen fuel* model and the *sloshing fuel* model that employs the neural network to replace slosh dynamics or the surrogate model or the bouncing ball model. Specifically, three different flight conditions are considered, that is $U_\infty = 130\,\mathrm{m/s}$ (corresponding approximately to the 80% of U_F) and $U_\infty = 160\,\mathrm{m/s}$, before the flutter margin as evaluated by the frozen fuel model, and $U_\infty = 168\,\mathrm{m/s}$ after the stability margin. Different gust intensities are employed to highlight the increase of the sloshing induced damping at high response amplitudes or the onset of limit cycle oscillations. In particular, Fig.12 shows comparisons of gust responses in the case where $U_\infty = 130, \mathrm{m/s}$ and for three different gust amplitudes w_{g_a}, respectively equal to $0.1\,\mathrm{m/s}$, $3\,\mathrm{m/s}$ and $5\,\mathrm{m/s}$. All comparisons will be shown in terms of the acceleration response at the free end of the beam. From Figs. 12(a),12(c) and 12(e), it is possible to appreciate how the presence of the neural network (representing the sloshing dynamics, defined in red as *sloshing fuel* in the graphs) contributes in providing a noticeable damping in the aeroelastic responses, if compared with those related to the frozen case. Surrogate model in Figs. 12(b), 12(d) and 12(f) is in line with the neural network based model but slight differences can be observed at $w_{g_a} = 0.1\,m/s$ in which the surrogate model seems to be more dissipative than neural networks. Moreover, in general Surrogate model provides an attenuation of the first peak less visible in neural network based model. This is a result of the quasi-static nature of the surrogate model not accounting for the initial fluid transient, *i.e.* the model instantly predicts the fluid is in the violent impacting and dissipative regime, without accounting for the initial period of energy input to excite free-surface waves. On the other hand the bouncing ball model looks to be ineffective in damping the structure at very low accelerations (in the range of accelerations in which no impacts occur). In the other cases, bouncing ball model seems to trigger the damping of the structure with a delayed mechanisms with respect to the other two models. Additionally, within Figs.12(d) and 12(f) higher frequency content of the other structural modes is excited in the bouncing ball response, resulting from the strong short-duration impacting nature of the EMM.

Then, the flight speed is brought close to the flutter margin, at a free stream velocity of $U_\infty = 160\,\mathrm{m/s}$, with a gust intensity of $w_{g_a} = 3\,\mathrm{m/s}$. Figure 13 compares the beam tip response of the sloshing fuel model with the frozen fuel model, for USRS in Fig. 13(a) and UB in Fig. 13(b).

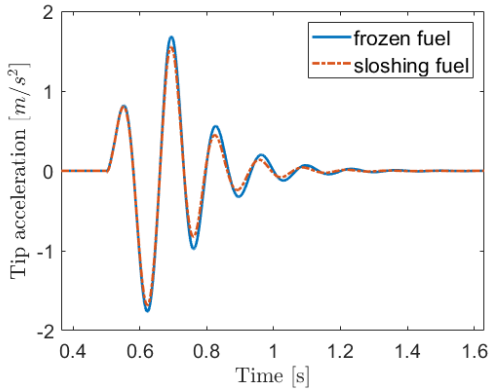

(a) USRS: $w_{g_a} = 0.1\,\mathrm{m/s}$

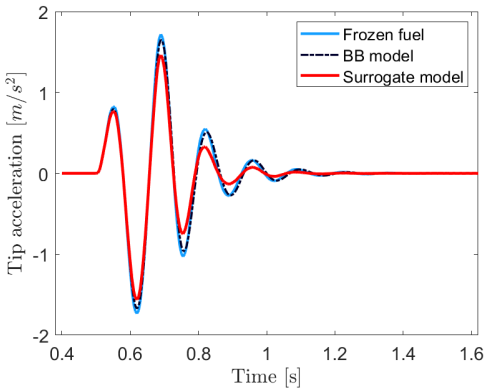

(b) UB: $w_{g_a} = 0.1\,\mathrm{m/s}$

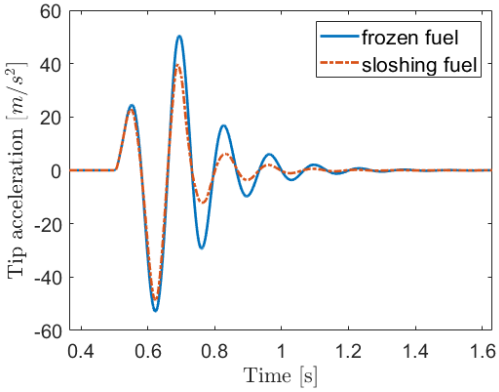

(c) USRS: $w_{g_a} = 3\,\mathrm{m/s}$

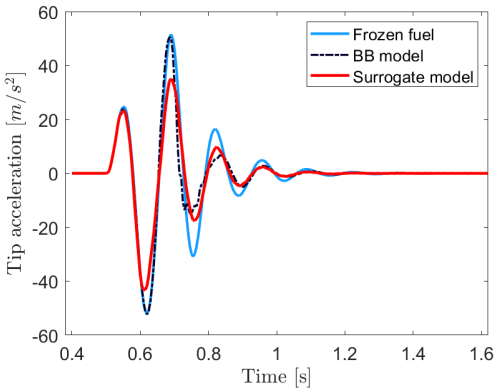

(d) UB: $w_{g_a} = 3\,\mathrm{m/s}$

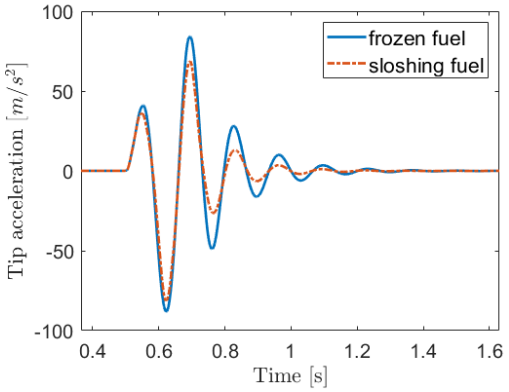

(e) USRS: $w_{g_a} = 5\,\mathrm{m/s}$

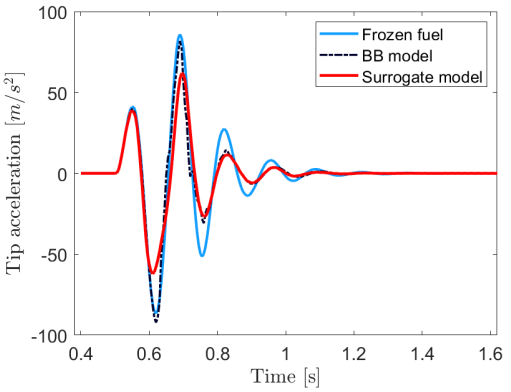

(f) UB: $w_{g_a} = 5\,\mathrm{m/s}$

Figure 12: Comparison of tip acceleration responses to a gust with different amplitudes w_{g_a}, between the frozen case and the sloshing case, for the University La Sapienza of Rome (USRS) and the University of Bristol (UB). The velocity is $U_\infty = 130\,\mathrm{m/s}$.

The damping induced by vertical sloshing dynamics aids in reducing the gust response even though the structure is closer to the flutter margin. However, in Fig. 13(b) the surrogate model appears less dissipative than the NN and has a region of low amplitude lightly damped response. This results from a lower aeroelastic damping in the frozen case, plus appears to have predicted a parametric sloshing regime, a result of the experimental data used, which poses much lower liquid damping than the initial violent transient. Furthermore, due to the nature of the bouncing-ball it shows dissipative characteristics that are more in line with a friction model [5], compared to the viscous like damping classically observed from liquid damping and correctly captured by the other models.

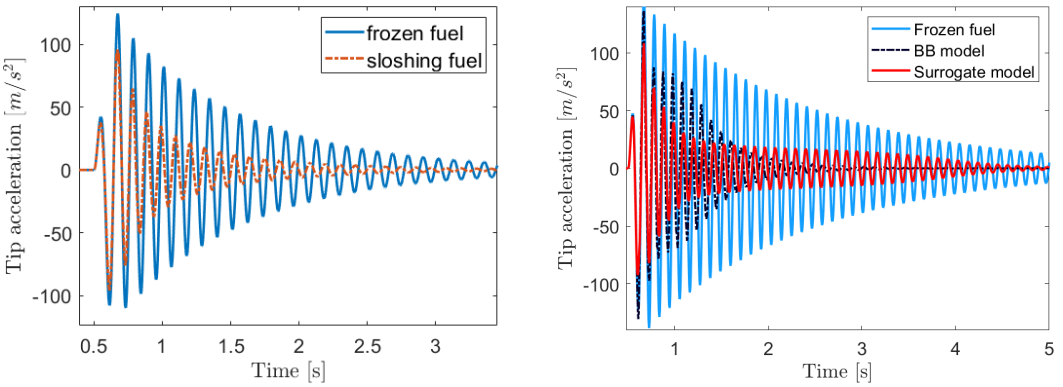

(a) USRS (b) UB

Figure 13: Comparison of gust responses in sub-critical condition for $U_\infty = 160\,\mathrm{m/s}$ and $w_{g_a} = 3\,\mathrm{m/s}$.

The post-critical gust response analysis is performed after the flutter speed limit at $U_\infty = 168\,\mathrm{m/s}$, with a gust intensity of $w_{g_a} = 0.1\,\mathrm{m/s}$. The beam tip response is shown in Fig. 13 comparing the two considered cases, again, highlighting the results obtained by USRS separately from those of UB (respectively shown in Fig. 14(a) and Fig. 14(b)). The linear frozen case results in a fluttering response with diverging exponential envelope, whilst the sloshing case develops a limit-cycle oscillation (LCO). This LCO is determined by the nature of the sloshing forces, which become highly dissipative when the acceleration of the tank increases.

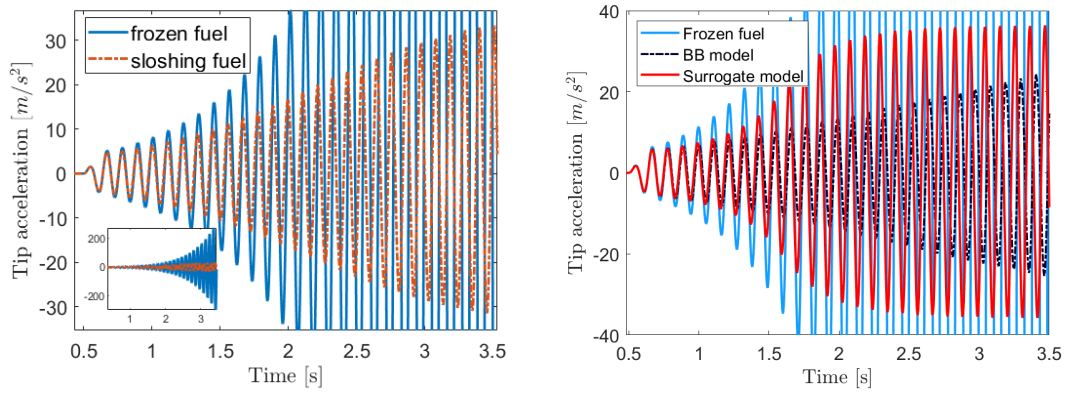

(a) USRS (b) UB

Figure 14: Comparison of gust responses in post-critical condition for $U_\infty = 168\,\mathrm{m/s}$ and $w_{g_a} = 0.1\,\mathrm{m/s}$.

Several response analyses for different velocities (before and after the flutter) have been per-

formed with the three considered models, collecting for each of them the value of the displacement at the tip of the wing at steady state, in order to estimate a bifurcation diagram. It is worth noticing that the amplitude of the deflections depends on the sloshing model as well as the aeroelastic modelling which already exhibits a slightly different critical speed without sloshing. Specifically the response analyses are carried out spanning free stream velocities from $160\,\mathrm{m/s}$ to $172\,\mathrm{m/s}$. Figures 15(a) and 15(b) show the Hopf bifurcation diagram of the limit-cycle oscillation of the wing tip displacement. Despite the nonlinear stabilising contribution of the sloshing forces, the system is nevertheless unstable for the three models after a flight speed slightly lower $173\,\mathrm{m/s}$ for the model with neural network and $167\,\mathrm{m/s}$ and $170\,\mathrm{m/s}$ respectively for the model with bouncing ball and surrogate model. This behaviour indicates the presence of an unstable branch at the same time as the stable one. It is worth noting that the range of existence of LCO is much lower for the bouncing ball model whereas the surrogate model presents an anticipation of flutter mechanism that involve a pre-critical behaviour.

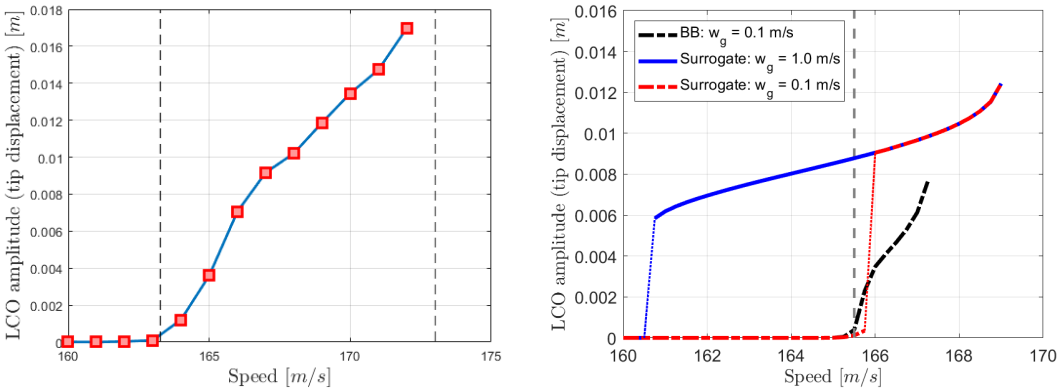

(a) USRS (b) UB

Figure 15: Comparison of bifurcation diagrams.

5 CONCLUSIONS

This work aimed at applying recently developed reduced-order sloshing models to study the aeroelastic response of the Goland wing model (considered as the representative aeroelastic testbed) to investigate the effects of sloshing on the wing's response under pre-critical and post-critical conditions. The vertical sloshing dynamics was considered using three different reduced order models: a neural-networks-based dynamical model, a bouncing ball and a further surrogate model trained with numerical and experimental data, and then integrated into the aeroelastic system.

In order to compare the three models, gust response analyses were carried out at varying amplitudes and for different flight conditions. The neural-network based ROM was trained by employing input/output data obtained by an experimental campaign carried out for the identification of the dissipative behaviour of a box tank when set on vertical motion. A tailored scaling procedure was then applied to account for the integration of the sloshing model into the considered aeroelastic system. On the other side, the bouncing ball model provides a quick and simple fluid model to implement, that is independent of scaling. This can capture coarse dissipative characteristics in some transient conditions, but struggles in regions of low acceleration excitation and the initial transient, plus introduces un-physical impulsive loading on the system. Finally, the surrogate model provides a balance between the bouncing ball and neural network. Requiring no calibration, it produces good dissipative behaviour with respect to the

higher-fidelity neural-network, but over-predicts damping during the initial transient due to the quasi-steady nature of the model.

The results showed how the three models representing vertical sloshing contributes to dampening the aeroelastic response, both in pre- and post-critical conditions. More in detail, after the onset of the dynamic instability, the all the three models are able, even with differences, to describe the existence of limit cycle oscillations for a limited range of flight speeds.

ACKNOWLEDGMENTS

This paper has been supported by SLOWD project. The SLOWD project has received funding from the European Union's Horizon 2020 research and innovation programme under grant agreement No 815044.

6 REFERENCES

[1] Gambioli, F., Chamos, A., Jones, S., et al. (2020). Sloshing Wing Dynamics -Project Overview Sloshing Wing Dynamics – Project Overview. In *Proceedings of 8th Transport Research Arena TRA 2020*.

[2] Benjamin, T. B., Ursell, F. J., and Taylor, G. I. (1954). The stability of the plane free surface of a liquid in vertical periodic motion. *Proceedings of the Royal Society of London. Series A. Mathematical and Physical Sciences*, 225(1163), 505–515.

[3] Gambioli, F., Usach, R. A., Wilson, T., et al. (2019). Experimental Evaluation of Fuel Sloshing Effects on wing dynamics. In *18th Int. Forum Aeroelasticity Struct. Dyn. IFASD 2019*.

[4] Titurus, B., Cooper, J. E., Saltari, F., et al. (2019). Analysis of a sloshing beam experiment. In *International Forum on Aeroelasticity and Structural Dynamics. Savannah, Georgia, USA*, vol. 139.

[5] Constantin, L., De Courcy, J., Titurus, B., et al. (2021). Analysis of damping from vertical sloshing in a sdof system. *Mechanical Systems and Signal Processing*, 152, 107452. ISSN 0888-3270.

[6] Firouz-Abadi, R. D., Zarifian, P., and Haddadpour, H. (2014). Effect of fuel sloshing in the external tank on the flutter of subsonic wings. *Journal of Aerospace Engineering*, 27(5), 04014021.

[7] Farhat, C., Chiu, E. K.-y., Amsallem, D., et al. (2013). Modeling of fuel sloshing and its physical effects on flutter. *AIAA Journal*, 51(9), 2252–2265.

[8] Colella, M., Saltari, F., Pizzoli, M., et al. (2021). Sloshing reduced-order models for aeroelastic analyses of innovative aircraft configurations. *Aerospace Science and Technology*, 118, 107075. ISSN 1270-9638.

[9] Hall, J., Rendall, T., and Allen, C. B. (2013). A two-dimensional computational model of fuel sloshing effects on aeroelastic behaviour. In *31st AIAA Applied Aerodynamics Conference*.

[10] Hall, J., Rendall, T., Allen, C., et al. (2015). A multi-physics computational model of fuel sloshing effects on aeroelastic behaviour. *Journal of Fluids and Structures*, 56, 11–32.

[11] Pizzoli, M., Saltari, F., Mastroddi, F., et al. (2022). Nonlinear reduced-order model for vertical sloshing by employing neural networks. *Nonlinear dynamics*, 107(2), 1469–1478.

[12] De Courcy, J. J., Constantin, L., Titurus, B., et al. (2021). Gust loads alleviation using sloshing fuel. In *AIAA Scitech 2021 Forum*.

[13] Constantin, L., De Courcy, J., Titurus, B., et al. (2021). Sloshing induced damping across froude numbers in a harmonically vertically excited system. *Journal of Sound and Vibration*, 510, 116302.

[14] Saltari, F., Pizzoli, M., Mastroddi, F., et al. (2022). Nonlinear sloshing integrated aeroelastic analyses of a research wing prototype. In *AIAA Scitech 2022 Forum*.

[15] Saltari, F., Pizzoli, M., Coppotelli, G., et al. (2022). Experimental characterisation of sloshing tank dissipative behaviour in vertical harmonic excitation. *Journal of fluids and structures*, 109, 103478.

[16] Goland, M. (1945). The flutter of a uniform cantilever wing. *Journal of Applied Mechanics*, 12(4), 197–208.

[17] Ahmad Fazelzadeh, S., Rezaei, M., and Mazidi, A. (2020). Aeroelastic analysis of swept pre-twisted wings. *Journal of Fluids and Structures*, 95, 103001. ISSN 0889-9746.

[18] Albano, E. and Rodden, W. P. (1994). Msc/nastran aeroelastic analysis' user's guide. *MSC Software*.

[19] Peters, D. A., Karunamoorthy, S., and Cao, W.-M. (1995). Finite state induced flow models. i-two-dimensional thin airfoil. *Journal of aircraft*, 32(2), 313–322.

[20] Pizzoli, M., Saltari, F., Coppotelli, G., et al. (2022). Experimental validation of neural-network-based nonlinear reduced-order model for vertical sloshing. In *AIAA Scitech 2022 Forum*.

[21] Wendland, H. (2004). *Scattered data approximation*, vol. 17. Cambridge university press.

[22] Nelles, O. (2021). *Nonlinear system identification, from classical approaches to neural networks, fuzzy models, and gaussian processes*. Springer, 2 ed.

[23] Beale, M. H., Hagan, M. T., and Demuth, H. B. (2020). *Deep Learning Toolbox*. Mathworks, r2020a ed.

[24] Martínez-Carrascal, J. and González-Gutiérrez, L. (2021). Experimental study of the liquid damping effects on a sdof vertical sloshing tank. *Journal of Fluids and Structures*, 100, 103172.

[25] Roger, K. L. (1977). Airplane math modeling methods for active control design.

COPYRIGHT STATEMENT